ChemComm

COMMUNICATION

View Article Online
View Journal | View Issue

Cite this: *Chem. Commun.*, 2025, **61**, 15393

Received 29th July 2025,
Accepted 2nd September 2025

DOI: 10.1039/d5cc04308e

rsc.li/chemcomm

Facet-dependent spatial charge separation in a metal-doped $SrTiO_3$ photocatalyst with visible light utilization

Xueshang Xin,[ab] Shiwen Du,[a] Yejun Xiao,[c] Hai Zou,[ab] Yunfeng Bao,[a] Yu Qi,[a] Shengye Jin,[c] Zhaochi Feng[a] and Fuxiang Zhang*[ab]

Visible-light-responsive Rh/Sb co-doped $SrTiO_3$ with engineered {100}/{110} facets (STO:RS(NaCl)) was synthesized *via* flux-assisted crystallization. Facet-dependent spatial charge separation, driven by work function differences, enabled electrons and holes to migrate to the respective facets. This configuration tripled photocatalytic hydrogen evolution *versus* non-faceted STO:RS(w/o), overcoming the limitations of ultraviolet-only absorption and inefficient charge separation.

Solar-driven water splitting using semiconductor photocatalysts offers sustainable energy solutions, yet efficient charge separation remains critical.[1] Rapid carrier recombination severely limits photocatalytic efficiency.[2,3] While cocatalyst deposition enhances carrier extraction,[4] traditional impregnation (imp.) or adsorption methods often yield randomly distributed cocatalysts with proximal redox sites, promoting electron–hole recombination. Controlled synthesis of anisotropic facets addresses this challenge by spatially separating electrons and holes,[5] as demonstrated in TiO_2, $BiVO_4$ and others.[6–8] Moreover, selective photodeposition of reduction/oxidation cocatalysts on electron/hole-rich facets further boosts carrier utilization efficiency and photocatalytic activity. Spatial separation of photogenerated carriers between the {100} and {110} facets of $BiVO_4$ led to a 17-fold enhancement in water oxidation activity after selective cocatalyst deposition.[9] Notably, anisotropic crystal facets exhibit distinct work functions, causing varied surface band bending and driving electron and hole migration in different spatial directions under the influence of the built-in electric field.[10] However, the synthesis of anisotropic facets remains challenging, limiting availability of photocatalysts with spatial charge separation, especially for metal ion-doped materials.

Since its initial report in 1980, $SrTiO_3$ (STO) has been extensively studied for photocatalysis.[11] Various strategies have been employed to enhance its photocatalytic performance,[12] including the induction of spatial charge separation through the exposure of anisotropic facets.[13,14] Domen *et al.* reported Al-modified STO with exposed {100}/{110} facets, which could selectively load dual cocatalysts on different facets, achieving nearly unity quantum efficiency.[10] However, the solar-to-hydrogen (STH) efficiency of STO remains <1% due to its UV-only response.[15] Doping is a commonly used and effective method to enhance the light-harvesting capacity and enable visible light response by introducing doping energy levels within the bandgap or modifying the valence band maximum (VBM) and conduction band minimum (CBM) positions through orbital hybridization.[16] Yet, controlling facets in metal-doped STO for extended visible-light utilization and their potential spatial charge separation remains understudied.

In this study, visible-light-responsive STO (STO:RS(NaCl)) with {100}/{110} facets was synthesized *via* Rh/Sb co-doping and NaCl flux treatment. Photodeposition confirmed the occurrence of spatial charge separation, while theoretical calculations revealed that anisotropic facet work function differences drive directional carrier migration. Photoluminescence (PL) and transient absorption spectroscopy (TAS) confirmed that spatial charge separation effectively enhances carrier utilization. Selective photodeposition of reduction/oxidation cocatalysts onto the respective {100}/{110} facets further enhanced carrier extraction and photocatalytic activity.

The synthesis route is schematically depicted in Fig. S1. Under high-temperature conditions in molten NaCl, STO:RS undergoes a continuous dissolution-recrystallization process. Na^+ ions adsorb onto the high-index facets, reducing surface free energy. According to crystal growth principles (Gibbs–Wulff theorem), the growth rate of a crystal facet is proportional to its surface energy. Consequently, the reduction in surface energy dramatically slows the growth kinetics and ultimately leads to the exposure of high-index facets.[17] The scanning electron microscopy (SEM) images showed that the STO:RS precursor particles

[a] *State Key Laboratory of Catalysis, Dalian National Laboratory for Clean Energy, Dalian Institute of Chemical Physics, Chinese Academy of Sciences, Dalian, 116023, China. E-mail: fxzhang@dicp.ac.cn*
[b] *Center of Materials Science and Optoelectronics Engineering, University of Chinese Academy of Sciences, Beijing, 100049, China*
[c] *State Key Laboratory of Molecular Reaction Dynamics, Dalian Institute of Chemical Physics, Chinese Academy of Sciences, Dalian, 116023, China*

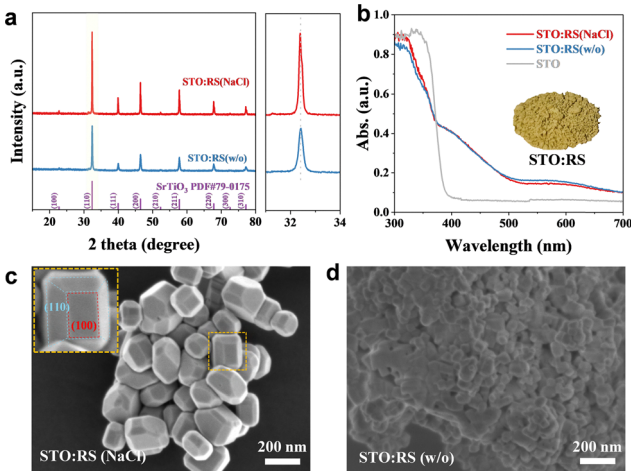

Fig. 1 (a) XRD patterns, (b) UV-vis DRS, and (c) and (d) SEM images of STO:RS(NaCl) and STO:RS(w/o).

(<50 nm, Fig. S2) underwent NaCl-assisted calcination to form faceted STO:RS(NaCl) with {100}/{110} exposure (Fig. 1c), whereas NaCl-free calcination yielded sintered STO:RS(w/o) with irregular morphology (Fig. 1d). Additionally, the high-angle annular dark-field scanning transmission electron microscopy (HAADF-STEM) images (Fig. S3) revealed a smooth surface structure and a highly ordered atomic arrangement from the surface to the bulk, confirming the single-crystalline nature of STO:RS(NaCl). The lattice spacings (0.39 nm and 0.28 nm) on adjacent facets and atomic arrangement directions corroborate that the exposed facets of STO:RS(NaCl) are {100} and {110}.

X-ray diffraction (XRD) patterns (Fig. 1a) for both STO:RS(w/o) and STO:RS(NaCl) were in good agreement with the cubic perovskite $SrTiO_3$ ($Pm\bar{3}m$, JCPDS no. 79-0175). Furthermore, Rietveld refinements were used to analyze the crystal structure of the two samples. As shown in Fig. S4 and Table S1, reasonable goodness-of-fit parameters were obtained when Rh, Sb and Ti occupy the same crystallographic positions. According to Vegard's law,[18] the calculated unit cell dimensions of STO:RS(NaCl) and STO:RS(w/o) showed only a limited difference compared to STO. This is attributed to the relative balance achieved by doping large-radius Rh^{3+} (0.665 Å) and small-radius Sb^{5+} (0.60 Å) ions into the Ti^{4+} (0.605 Å) sites.[19] Inductively coupled plasma optical emission spectrometry (ICP-OES) analysis (Table S2) verified that the Rh and Sb concentrations in both STO:RS(NaCl) and STO:RS(w/o) were comparable. X-ray photoelectron spectra (XPS) analysis further demonstrated that the valence states of Rh, Sb and Ti in both samples were nearly the same (Fig. S5). The above results indicated that Rh and Sb were successfully doped into STO:RS(NaCl) and STO:RS(w/o).

UV-vis diffuse reflectance spectra (DRS) revealed visible-light absorption in both STO:RS(NaCl) and STO:RS(w/o) (Fig. 1b), contrasting with UV-only absorption in pristine STO. These absorption bands could respectively be assigned to Rh^{3+} → CBM transitions (390–520 nm) and VBM → Rh^{4+} transitions (~580 nm). Notably, Sb^{5+} does not affect the light absorption of STO, but only reduces the presence of Rh^{4+} through charge balance.[20] Density functional theory (DFT) simulations (Fig. S6) revealed that Rh doping introduces new energy levels within the bandgap, while Sb leaves band edges unaffected. Additionally, STO:RS maintains pristine STO's indirect bandgap characteristic. Tauc plots showed comparable bandgaps (~2.44 eV) for both samples (Fig. S7a). Mott–Schottky (MS) analysis (Fig. S7b) revealed a more negative flat-band potential for STO:RS(NaCl) (−0.18 eV *vs.* −0.12 eV for STO:RS(w/o)), which was attributed to exposed facet differences.[21] The positive curve slope confirms n-type behavior, where CBM is typically 0.1–0.2 eV above the flat-band potential,[22] with bandgaps obtained from Tauc plots, and the VBM and CBM were estimated (Fig. S7c).

The facet-dependent spatial charge separation in STO:RS(NaCl) was systematically investigated through redox-selective photodeposition ($\lambda \geq 420$ nm, Fig. 2a–f). Metal oxides (CoOOH and MnO_x) were preferentially accumulated on the {110} facet (hole-rich),[23] while metals (Pt/Ag/Au) were selectively deposited on the {100} facet (electron-rich). Energy dispersive X-ray spectroscopy (EDS) mappings of the Ag/STO:RS(NaCl) and MnO_x/STO:RS(NaCl) (Fig. S8) showed that the Ag and MnO_x were successfully deposited on the surface, respectively. XPS analysis further confirmed the presence of metals and metal oxides (Fig. S9). According to the binding energy, both Ag and Au were in metallic form, while Co and Mn existed in the form of CoOOH and MnO_x ($1.5 < x < 2$). Notably, platinum exhibited incomplete reduction with coexisting metallic Pt and partially reduced Pt(II)O species, which was consistent with previously reported Pt(IV) reduction characteristics.[13] These results directly correlated facet electronic properties with redox selectivity. As a comparison, impregnation-loaded Pt on STO:RS(NaCl) showed a random distribution (Fig. S10a), ruling out thermodynamic adsorption preference as the cause of facet selectivity. In addition, Pt showed random deposition orientation and was independent of the deposition method (Fig. S11),

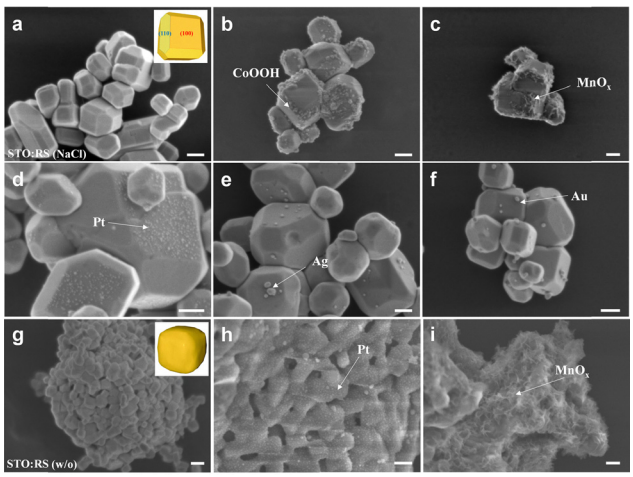

Fig. 2 SEM images of (a) STO:RS(NaCl) and STO:RS(NaCl) loaded with (b) CoOOH, (c) MnO_x, (d) Pt, (e) Ag, and (f) Au by photodeposition. SEM images of (g) STO:RS(w/o) and STO:RS(w/o) loaded with (h) Pt and (i) MnO_x by photodeposition; the scale is 100 nm.

ruling out lattice matching or epitaxial effects. Furthermore, dual MnO_x/Au photodeposition validated charge rectification, with MnO_x on {110} and Au on the {100} facet, achieving spatial separation of dual species on the surface (Fig. S10b). In contrast, irregular STO:RS(w/o) showed random Pt/MnO_x distributions (Fig. 2g–i). This contrast stemmed from divergent carrier dynamics: anisotropic facets in STO:RS(NaCl) enabled directional transport, whereas disordered STO:RS(w/o) permitted random migration.

PL and TAS analyses revealed enhanced charge separation in faceted STO:RS(NaCl). Steady-state PL spectra exhibited broad emission bands ranging from 400 to 650 nm, with a peak at 440 nm (Fig. S12a and b), originating from the recombination of photogenerated carriers. Based on the time-resolved photoluminescence (TRPL) decay spectra and fitting results (Fig. 3a, b and Table S3), STO:RS(NaCl) exhibited a shorter average carrier lifetime (τ_{AV} = 0.89 ns *vs.* 1.16 ns for STO:RS(w/o)), indicating that the faceted material exhibited enhanced non-radiative charge extraction compared to radiative recombination pathways.[24] TAS revealed significant differences in trap-state dynamics (Fig. 3c and d). STO:RS(NaCl) showed 56% weaker defect absorption ($\Delta A = 0.8 \times 10^{-3}$ *vs.* 1.8×10^{-3} for STO:RS(w/o)) at 650 nm, attributed to Rh^{4+}-related traps.[25] Cocatalyst modification further reduced the defect-induced absorption (Fig. S12c and d). Specifically, the residual trapping signal was attenuated by 50% upon Pt and CoOOH modified STO:RS(NaCl). The collective evidence confirms that anisotropic facet direct carriers prefer separation transfer rather than being trapped in defect states. Surface photovoltage (SPV) spectroscopy (Fig. S13) provided direct evidence about the surface charge accumulation.[26,27] It was found that STO:RS(NaCl) exhibited a six-fold stronger SPV signal than STO:RS(w/o). Moreover, Pt/CoOOH loading further enhanced SPV (Fig. S13b), confirming that spatial separation of photogenerated charges allowed for faster and more efficient charge transfer to the material's surface and that the loading of cocatalysts can further enhance this effect. DFT simulations (Fig. 3e and f) revealed that the work functions of the {100} and {110} facets were 3.15 eV and 5.66 eV, respectively. The higher work function of {110} induced more pronounced surface band bending compared to {100}, generating a stronger built-in electric field in its space charge region that drove holes to accumulate on {110} and electrons on {100} (Fig. S14).[28] The resulting spatial charge separation creates distinct redox environments: hole-rich {110} favors oxidation (forming metal oxides), while electron-rich {100} favors reduction (forming metals).

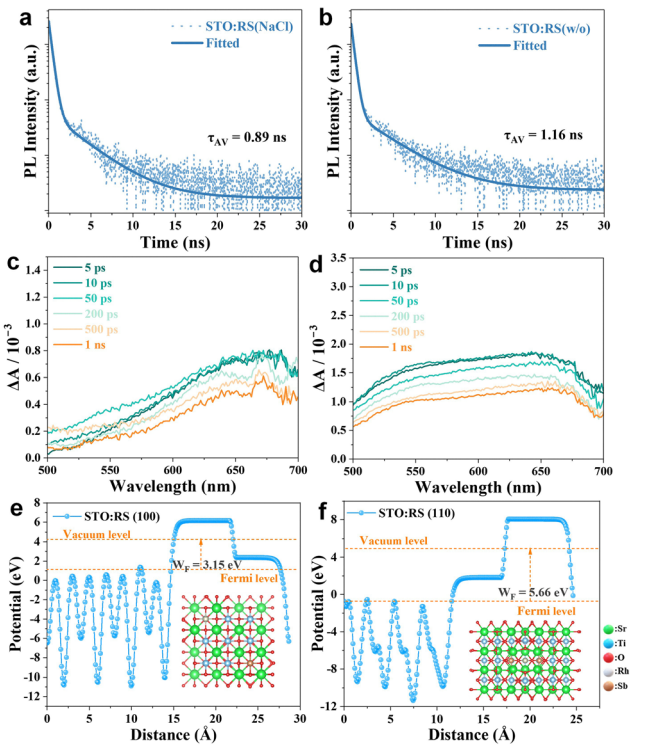

Fig. 3 TRPL decay curves of (a) STO:RS(NaCl) and (b) STO:RS(w/o) measured at 440 nm. TAS of (c) STO:RS(NaCl) and (d) STO:RS(w/o). Theoretical calculated work functions of the (e) {100} and (f) {110} facets of STO:RS(NaCl).

The photocatalytic hydrogen evolution reaction (HER) is a crucial process where charge separation is mostly identified as the rate-limiting step.[2] In the case of STO:RS(NaCl), Pt was used as a HER cocatalyst and methanol as the sacrificial reagent. Photodeposited Pt on the electron-rich {100} facet achieved twice the HER activity (3.1 *vs.* 1.7 μmol h^{-1}) compared to randomly distributed Pt *via* impregnation (Fig. S15). A CoOOH oxidation cocatalyst was photodeposited on the {110} facet to synergistically enhance hole extraction. Loading dual-cocatalysts (0.50 wt% Pt and 0.75 wt% CoOOH) significantly boosted the HER activity by 2.7-fold compared to single-cocatalyst (0.50 wt% Pt) systems (Fig. 4a). Based on Fig. S16 validation, optimal cocatalyst loading showed a volcano-shaped activity trend. With 0.5 wt% Pt fixed, activity peaked at 0.75 wt% CoOOH for STO:RS(NaCl). The same trend occurred reciprocally (fixed 0.75 wt% CoOOH, varying Pt). This indicates that moderate loading enhances charge extraction and reaction sites, while excess cocatalysts block light and hinder activity.

Pristine STO:RS(NaCl) and STO:RS(w/o) exhibited negligible HER activity (Fig. 4b), but after photodeposition of dual cocatalysts (0.50 wt% Pt and 0.75 wt% CoOOH), STO:RS(NaCl) achieved three times higher HER rate (9.2 *vs.* 2.9 μmol h^{-1}) than STO:RS(w/o), despite identical Rh/Sb doping (ICP-OES) and light absorption (UV-vis DRS). This superior performance of STO:RS(NaCl) was attributed to the directional migration of photogenerated electrons and holes, which effectively improved the carrier separation efficiency. In the linear sweep voltammetry (LSV) test, STO:RS(NaCl) exhibited a higher photocurrent compared to STO:RS(w/o) (Fig. S17a). After spatially selective photodeposition, Pt–CoOOH/STO:RS(NaCl) exhibited the highest photocurrent response, suggesting that the loading of dual-cocatalysts could extract carriers more effectively (Fig. S17b). In addition, the smaller Nyquist curve radius in the electrochemical impedance spectroscopy (EIS) test for STO:RS(NaCl) demonstrated lower charge transfer resistance compared to STO:RS(w/o) (Fig. S17c). HER stability was confirmed through cyclic tests (Fig. 4c) with consistent performance, and the

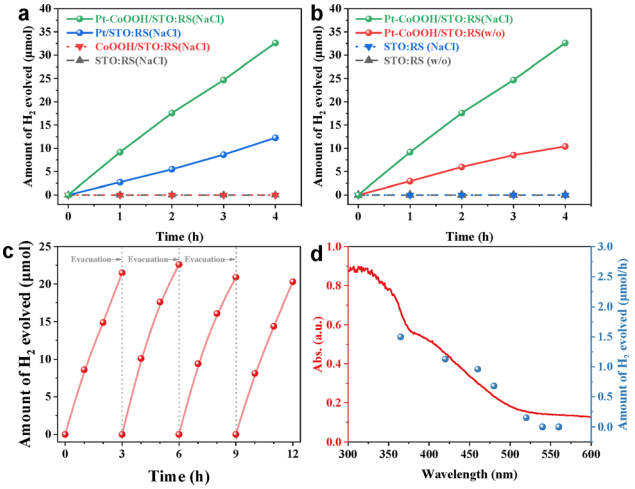

Fig. 4 (a) HER on STO:RS(NaCl) loaded with different cocatalysts *via* photodeposition. (b) HER on STO:RS(NaCl) and STO:RS(w/o) with or without Pt/CoOOH loaded. (c) Curves of multiple cycles of activity as a function of reaction time. (d) Wavelength dependence of the HER.

post-reaction STEM analysis (Fig. S18) showed that the STO:RS(NaCl) retained its single-crystalline structure, while the Pt cocatalyst maintained intimate interfacial contact with STO. Wavelength dependence experiments (Fig. 4d) demonstrated that photocatalytic hydrogen production was directly linked to light absorption.

In summary, we demonstrated a visible-light-active $SrTiO_3$ photocatalyst (STO:RS(NaCl)) with facet-dependent charge separation, synthesized *via* Rh/Sb co-doping and NaCl flux treatment. Systematic characterization (photodeposition, PL, TAS, SPV) confirmed that electrons and holes migrate to {100} and {110} facets, respectively, and facilitate the improvement of carrier separation efficiency, which was driven by facet-specific work function differences. The photocatalytic hydrogen evolution of STO:RS(NaCl) is three times higher than that of STO:RS(w/o). The work established a dual strategy – doping for visible absorption and facet engineering for charge rectification – providing a blueprint for designing efficient solar-driven semiconductors.

This work was supported by the National Natural Science Foundation of China (21925206, 22409022), Dalian Supports High-level Talent Innovation and Entrepreneurship Projects (2020RD06), and the Liaoning Revitalization Talents Program (XLYC1807241).

Conflicts of interest

There are no conflicts to declare.

Data availability

The data supporting this article have been included as part of the SI. See DOI: https://doi.org/10.1039/d5cc04308e.

Notes and references

1 X. Tao, Y. Zhao, S. Wang, C. Li and R. Li, *Chem. Soc. Rev.*, 2022, **51**, 3561–3608.
2 Y. Xu, A. Li, T. Yao, C. Ma, X. Zhang, J. H. Shah and H. Han, *ChemSusChem*, 2017, **10**, 4277–4305.
3 X. Guan, S. Zong and S. Shen, *Nano Res.*, 2022, **15**, 10171–10184.
4 J. Yang, D. Wang, H. Han and C. Li, *Acc. Chem. Res.*, 2013, **46**, 1900–1909.
5 S. Wang, G. Liu and L. Wang, *Chem. Rev.*, 2019, **119**, 5192–5247.
6 H. G. Yang, C. H. Sun, S. Z. Qiao, J. Zou, G. Liu, S. C. Smith, H. M. Cheng and G. Q. Lu, *Nature*, 2008, **453**, 638–641.
7 Y. Deng, H. Zhou, Y. Zhao, B. Yang, M. Shi, X. Tao, S. Yang, R. Li and C. Li, *Small*, 2022, **18**, 2103245.
8 J. Zhang, K. Liu, B. Zhang, J. Zhang, M. Liu, Y. Xu, K. Shi, H. Wang, Z. Zhang, P. Zhou and G. Ma, *J. Am. Chem. Soc.*, 2024, **146**, 4068–4077.
9 R. Li, H. Han, F. Zhang, D. Wang and C. Li, *Energy Environ. Sci.*, 2014, **7**, 1369–1376.
10 T. Takata, J. Jiang, Y. Sakata, M. Nakabayashi, N. Shibata, V. Nandal, K. Seki, T. Hisatomi and K. Domen, *Nature*, 2020, **581**, 411–414.
11 K. Domen, S. Naito, M. Soma, T. Onishi and K. Tamaru, *J. Chem. Soc., Chem. Commun.*, 1980, 543–544.
12 T. Takata and K. Domen, *J. Phys. Chem. C*, 2009, **113**, 19386–19388.
13 L. Mu, Y. Zhao, A. Li, S. Wang, Z. Wang, J. Yang, Y. Wang, T. Liu, R. Chen, J. Zhu, F. Fan, R. Li and C. Li, *Energy Environ. Sci.*, 2016, **9**, 2463–2469.
14 Y. Zhang, X. Wu, Z.-H. Wang, Y. Peng, Y. Liu, S. Yang, C. Sun, X. Xu, X. Zhang, J. Kang, S.-H. Wei, P. F. Liu, S. Dai and H. G. Yang, *J. Am. Chem. Soc.*, 2024, **146**, 6618–6627.
15 H. Nishiyama, T. Yamada, M. Nakabayashi, Y. Maehara, M. Yamaguchi, Y. Kuromiya, Y. Nagatsuma, H. Tokudome, S. Akiyama, T. Watanabe, R. Narushima, S. Okunaka, N. Shibata, T. Takata, T. Hisatomi and K. Domen, *Nature*, 2021, **598**, 304–307.
16 Z. Pan, J. J. M. Vequizo, H. Yoshida, J. Li, X. Zheng, C. Chu, Q. Wang, M. Cai, S. Sun, K. Katayama, A. Yamakata and K. Domen, *Angew. Chem., Int. Ed.*, 2025, **64**, e202414628.
17 H. Kato, M. Kobayashi, M. Hara and M. Kakihana, *Catal. Sci. Technol.*, 2013, **3**, 1733–1738.
18 A. R. Denton and N. W. Ashcroft, *Phys. Rev. A: At., Mol., Opt. Phys.*, 1991, **43**, 3161–3164.
19 R. Shannon, *Acta Crystallogr., Sect. A*, 1976, **32**, 751–767.
20 R. Niishiro, S. Tanaka and A. Kudo, *Appl. Catal., B*, 2014, **150–151**, 187–196.
21 S. Assavachin, C. Xiao, K. Becker and F. E. Osterloh, *Energy Environ. Sci.*, 2024, **17**, 3493–3502.
22 Y. Matsumoto, *J. Solid State Chem.*, 1996, **126**, 227–234.
23 H. Lyu, T. Hisatomi, Y. Goto, M. Yoshida, T. Higashi, M. Katayama, T. Takata, T. Minegishi, H. Nishiyama, T. Yamada, Y. Sakata, K. Asakura and K. Domen, *Chem. Sci.*, 2019, **10**, 3196–3201.
24 Y. Deng, Q. Li, P. Wang, F. Sun, C. Li and R. Li, *Catal. Sci. Technol.*, 2024, **14**, 4228–4235.
25 J. J. M. Vequizo, S. Nishioka, J. Hyodo, Y. Yamazaki, K. Maeda and A. Yamakata, *J. Mater. Chem. A*, 2019, **7**, 26139–26146.
26 Y. Li, Z. Liu, J. Li, M. Ruan and Z. Guo, *J. Mater. Chem. A*, 2020, **8**, 6256–6267.
27 Q. Wang, X. Zhan, C. Fan, X. Yang, B. Li, H. Liu, Y. Wu, K. Zhang and P. Tang, *J. Mater. Chem. A*, 2024, **12**, 33290–33300.
28 S.-C. Chan, Y.-L. Cheng, B. K. Chang and C.-W. Hong, *RSC Adv.*, 2021, **11**, 18500–18508.